Fe_7S_8 nanoparticles encapsulated in porous N, S co-doped carbon as an efficient bifunctional electrocatalyst for Zn-air battery

Tongzhou Jiang, Peng Dai ✉, *Wen Zhang*

School of Physics and Materials Science, Anhui University, Hefei 230601, People's Republic of China
✉ *E-mail: daipeng@mail.ustc.edu.cn*

Published in Micro & Nano Letters; Received on 12th December 2019; Revised on 1st March 2020; Accepted on 18th March 2020

The development of low-cost and highly active bifunctional electrocatalysts for oxygen reduction reaction (ORR) and oxygen evolution reaction (OER) is of great significance to promote the practical application of Zn-air battery (ZAB). Herein, the authors report a facile strategy for the fabrication of Fe_7S_8 nanoparticles embedded in the N, S co-doped porous carbon (NSC) network that served as an efficient bifunctional catalyst. The obtained Fe_7S_8/NSC shows remarkable oxygen electrocatalytic activity, in terms of superior ORR activity to commercial Pt/C as well as comparable OER capability to RuO_2. Besides, when evaluated as the cathode catalyst for a homemade ZAB, Fe_7S_8/NSC also displays a superior peak power density of 135 mA cm^{-2} and high cycling stability over 65 h (195 cycles).

1. Introduction: With the fast consumption of fossil fuels, tremendous efforts have been applied to the development of highly efficient energy generation and storage systems to relieve the increasing global energy crisis. Zn-air battery (ZAB) is emerging as the most promising energy storage device for flexible electronics, because of its high theoretical special energy (1086 Wh kg^{-1}), low price and high safety [1]. However, the conversion efficiency of ZAB is hampered by the unsatisfactory electrochemical performance of the air cathode, which is mainly attributed to the sluggish oxygen reduction reaction (ORR) and oxygen evolution reaction (OER) kinetics [2]. Although noble metal-based catalysts such as Pt-based and Ru-/Ir-based materials are served as the state-of-the-art catalysts in ZABs, the high cost and poor durability limit their application prospects [3]. Therefore, it is highly desired to develop bifunctional electrocatalysts for both ORR and OER with efficient activity, low price, and superior stability.

Transition metal sulphides, as a new type of non-precious electrocatalysts, have attracted substantial attention as advanced electrode materials for their abundance, high activity, and good stability [4]. Despite the progress, transition metal chalcogenides suffer from low electrical conductivity, poor distribution, and nanoparticle agglomeration, leading to inferior electrocatalytic performance. Recently, introducing transition metal sulphides into heteroatom-doped carbon materials to form a composite is considered as the most investigated technology, which can effectively improve the electrocatalytic activity and stability on account of the large specific surface area, great stability and high conductivity of carbon matrix [5]. Moreover, the presence of heteroatoms such as nitrogen and sulphur atoms will modify the electronic structures of carbon frameworks, form more defects, and offer more active sites, then remarkably boost the ORR and OER activity [6].

Driven by these hints, we firstly synthesised 3D N, S co-doped interconnected porous carbon matrix (NSC) using SiO_2 nanospheres as the precursors. Subsequently, the Fe_7S_8 nanoparticles were successfully embedded into the NSC framework with the ionic adsorption process and the following calcination strategy. As expected, the as-obtained Fe_7S_8/NSC catalyst exhibits outstanding electrocatalytic activity and durability in ORR/OER, which is mainly ascribed to the distinctive 3D interconnected porous networks, the doping of nitrogen and sulphur atoms, and the synergistic interaction between Fe_7S_8 and carbon matrix. Moreover, the primary homemade ZAB based on Fe_7S_8/NSC catalyst demonstrated a higher peak power density and better durability than those of Pt/C–RuO_2 mixed catalysts, signifying the substantial application prospect as an efficient bifunctional catalyst in ZAB.

2. Experimental details

2.1. Synthesis of Fe_7S_8/NSC: Typically, 1.0 g of glucose, 1.0 g of thiourea, and 2.0 g of SiO_2 nanospheres were first ground thoroughly in an agate mortar. Then, the mixture was dried, and calcined in a tube furnace at 850°C under an N_2 atmosphere for 2 h. Subsequently, the obtained powders were uniformly dispersed into a 2 M NaOH solution, kept at 60°C for 8 h to remove the SiO_2 template. Finally, NSC nanoparticles were obtained after the process of centrifugation, washing with absolute ethanol and drying at 50°C for 12 h.

For the preparation of Fe_7S_8/NSC, 0.1 g of NSC and 0.15 g of $FeCl_3{\cdot}6H_2O$ were first dissolved in the solution containing 40 ml of dimethylformamide and 10 ml of deionised water, and stirred to form a homogeneous solution. Then, the above mixture was poured into a Teflon-lined autoclave, kept at 80°C for 2 h. The resultant precipitates were washed and dried at 50°C for 12 h. After being calcined in a tube furnace at 900°C for 2 h, the as-fabricated sample was labelled as Fe_7S_8/NSC. Moreover, Fe_7S_8 nanoparticles were fabricated based on [7] for comparative catalytic studies, denoted as sample Fe_7S_8.

2.2. Characterisation of the samples: The structures and morphologies of the as-prepared catalysts were examined by using an X-ray diffractometer (XRD, Bruker D8-ADVANCE), field-emission scanning electron microscope (FE-SEM, S-4800), transmission electron microscopy (TEM, JEM-2100), and X-ray photoelectron spectroscope (XPS, PHI-5702 instrument with Al Kα radiation). The Raman spectroscopy was recorded on a Raman spectrometer (inVia-Reflex, Renishaw), and the nitrogen adsorption/desorption isotherms were investigated at 77 K (3H-2000PS2, BeiShiDe Instrument). Moreover, the element concentrations of samples were tested by using an inductively coupled plasma-atomic emission spectrometer (ICP-AES, Optima 7400 DV).

All electrochemical tests of ORR/OER performances were analysed using a CHI 760E electrochemical workstation. The electrode preparation was carried out as follows: 8 µl of ink (5 mg/ml) was dropped onto a rotating disk electrode made up of glassy carbon, with a diameter of 5 mm, then dried thoroughly at room temperature. Moreover, a homemade ZAB was built using a Zn flake as the anode, Fe_7S_8/NSC catalyst applied on the carbon cloth as

the air cathode, and the mixture of KOH (6.0 M) and $Zn(Ac)_2$ (0.2 M) as the electrolyte. The tests of ZABs were measured by using the LAND Battery Testing System (LAND-CT2001A).

3. Results and discussion: The morphologies and microstructures of resultant samples were first analysed by SEM. As shown is Fig. 1*a*, sample NSC exhibits an alveolate porous structure, comprised interconnected holes with a diameter of ~100–200 nm. There is an obvious agglomeration of Fe_7S_8 nanoparticles in Fig. 1*b*, with the particle distribution in the range of 100–400 nm. While for sample Fe_7S_8/NSC, Fe_7S_8 nanoparticles are homogeneously distributed on the NSC, with sizes of 20–100 nm. Moreover, the sample Fe_7S_8/NSC still maintains the same structure with NSC even after embedding Fe_7S_8 nanoparticles into the carbon matrix. Fig. 2*a* further illustrates the TEM image of sample Fe_7S_8/NSC, also confirming the maintenance of the distinctive 3D interconnected porous structure, in which the black spots on NSC are supposed to be Fe_7S_8 nanoparticles. In addition, Fig. 2*b* shows the high-resolution TEM (HRTEM) image of sample Fe_7S_8/NSC. The lattice fringe spacing of around 0.265 nm is well assigned to the (203) plane of Fe_7S_8 [8], suggesting the existence of Fe_7S_8 nanoparticles in the NSC framework.

The graphitisation degree of resultant samples was characterised through XRD and Raman spectra. As can be seen in Fig. 3*a*, the XRD pattern of NSC has a broad peak at around 24° denoted by the typical (002) plane of graphitic carbon, signifying the amorphous carbon structure of NSC [9]. For Fe_7S_8 and Fe_7S_8/NSC, the strong diffraction peaks at 2θ values of 29.8, 33.9, 43.6, 53.1, 57.0, 64.6, 70.8, and 73.1 are attributed to the (200), (203), (206), (220), (209), (0012), (406), and (411) planes, respectively, of Fe_7S_8 (JCPDS card no. 25–0411). Thus the XRD results revealed the successful fabrication of Fe_7S_8/NSC composites. The Raman spectra in Fig. 3*b* show two characteristic peaks at about 1349 and 1579 cm^{-1} for both NSC and Fe_7S_8/NSC, assigned to the typical D band and G band of carbon materials, respectively. Interestingly, the I_G/I_D ratio of Fe_7S_8/NSC (0.97) is higher than that of NSC (0.93), indicating that the introduction of Fe_7S_8 into NSC can cause more defects [10]. Thus, more active cites are conductive to be generated in the interior of the carbon skeleton, in favour of the catalytic activity.

Nitrogen adsorption–desorption measurements were employed to analyse the surface area of samples NSC, Fe_7S_8, and Fe_7S_8/NSC.

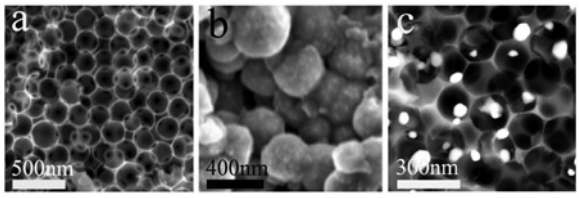

Fig. 1 *Typical SEM images of*
a NSC
b Fe_7S_8
c Fe_7S_8/NSC

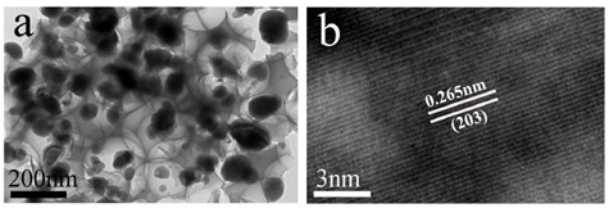

Fig. 2 *Typical TEM and HRTEM images of Fe_7S_8/NSC*
a TEM image of Fe_7S_8/NSC
b HRTEM image of Fe_7S_8/NSC

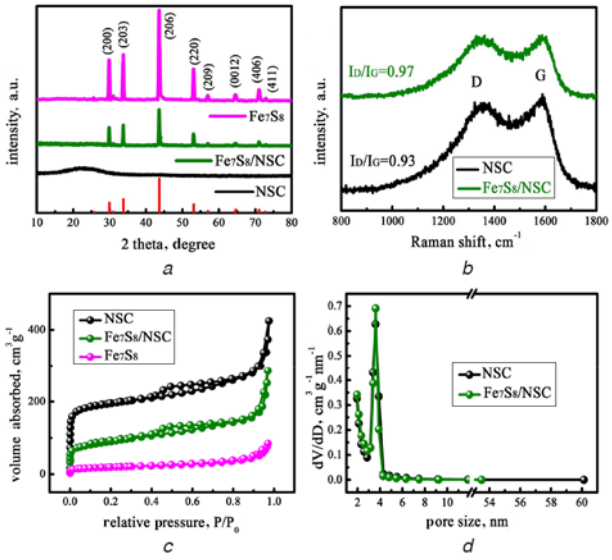

Fig. 3 *Characteristics of NSC, Fe_7S_8, and Fe_7S_8/NSC*
a XRD patterns
b Raman spectra
c N_2 adsorption–desorption isotherms
d Corresponding pore size distribution

As illustrated in Fig. 3*c*, samples NSC and Fe_7S_8/NSC exhibit the same IV adsorption/desorption isotherm curves, accompanied by a typical hysteresis loop (H3 type), demonstrating the existence of mesoporous architecture [11]. Moreover, the specific surface area value of Fe_7S_8 is calculated as 15.7 m^2 g^{-1}, much smaller than that of NSC (601.2 m^2 g^{-1}) and Fe_7S_8/NSC (301.3 m^2 g^{-1}). The pore size of NSC and Fe_7S_8/NSC could be further determined from the adsorption branch, which is mainly distributed over the range of 2.83–4.32 and 2.87–4.27 nm (Fig. 3*d*), respectively, suggesting the presence of mesoporosity. Most notably, the mesoporous structures and relatively large specific areas of NSC and Fe_7S_8/NSC are contributing to the exposure of more active sites and the rapid transport of electrons, thus resulting in the excellent catalytic activity of catalysts. In addition, inductively coupled plasma-atomic emission spectrometry (ICP-AES) were conducted to determine the iron and sulphur concentrations in Fe_7S_8/NSC, and the weight percentages of Fe and S are 12.53 and 9.14 wt%, respectively. Based on the value of Fe element, the content of Fe_7S_8 nanoparticles in Fe_7S_8/NSC is estimated to be 20.71 wt%.

The XPS measurement was further implemented to characterise the surface chemical valence and composition of sample Fe_7S_8/NSC. The high-resolution C 1s spectrum in Fig. 4*a* can be split into four peaks located at 284.6, 285.3, 286.4, and 288.3 eV, corresponding to C–C=C, C–S–C, C–N–C, and C=O bond, respectively [5]. Fig. 4*b* further gives the spectrum of the N 1s, and the binding energies at about 398.5, 400.2, and 401.3 eV can be assigned to pyridinic N, pyrrolic N, and graphite N, respectively. As shown in Fig. 4*c*, S 2p spectra are mainly deconvoluted into four peaks at about 163.7, 164.8, 168.4, and 169.6 eV. The peaks at 163.7 and 164.8 eV can be assigned to S 2p1/2 and S 2p3/2, while the rest two peaks at 168.4 and 169.6 eV are relevant to the highly oxidised sulphur species [5]. As to the Fe 2p spectrum in Fig. 4*d*, two spin–orbit doublets at 724.3 and 725.9 eV, and at 711.2 and 713.7 eV are well attributed to Fe 2p1/2, and Fe 2p3/2, respectively. Meanwhile, two satellite peaks are discovered at 719.1 and 732.8 eV [12]. Therefore, the desirable interconnected porous network structure and the optimised surface chemical composition make Fe_7S_8/NSC attractive as an efficient oxygen electrocatalyst.

To evaluate the catalytic behaviour of as-synthesised catalysts, the linear sweep voltammetry (LSV) instruments were first employed, shown in Fig. 5*a*. As expected, Fe_7S_8/NSC shows

doi: 10.1049/mnl.2019.0763

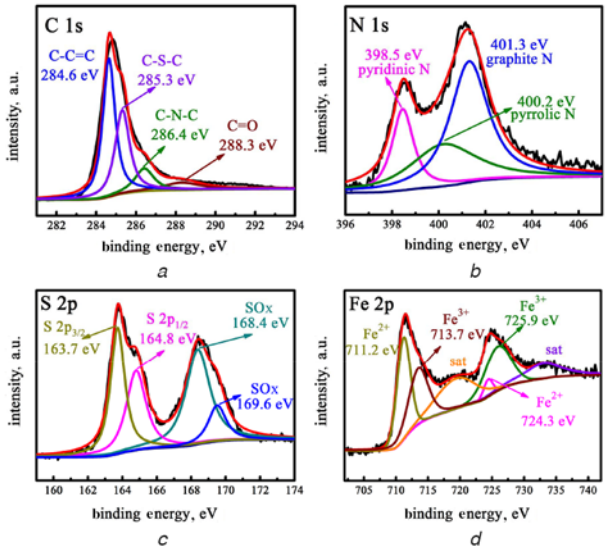

Fig. 4 *XPS spectra of Fe_7S_8/NSC*
a C 1s
b N 1s
c S 2p
d Fe 2p

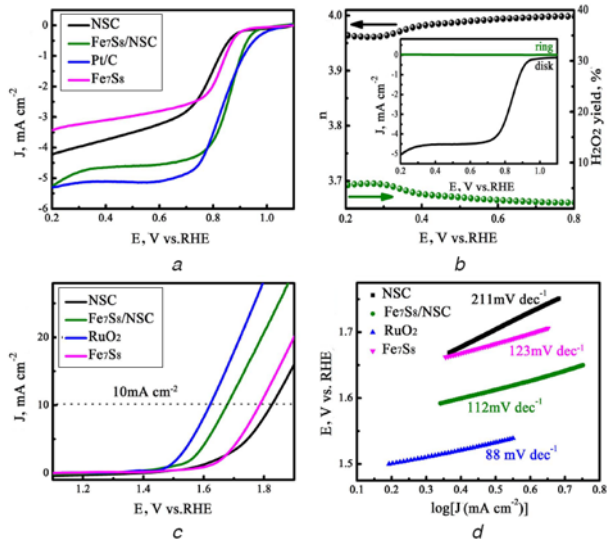

Fig. 5 *Electrochemical performances of all samples*
a LSV of NSC, Fe_7S_8, Fe_7S_8/NSC, and Pt/C at a rotating rate of 1600 rpm in O_2-saturated 0.1 M KOH for ORR
b Peroxide yield and electron transfer number of Fe_7S_8/NSC obtained by RRDE voltammetry in O_2-saturated 0.1 M KOH
c LSV for OER of NSC, Fe_7S_8, Fe_7S_8/NSC, and RuO_2
d Tafel plots of NSC, Fe_7S_8, Fe_7S_8/NSC, and RuO_2

excellent ORR performance with a half-wave potential ($E_{1/2}$) value of 0.85 V, significantly outperforming those of NSC ($E_{1/2}=0.77$ V), Fe_7S_8 ($E_{1/2}=0.81$ V), and even that of Pt/C ($E_{1/2}=0.83$ V). In addition, the rotating ring disk electrode (RRDE) tests were applied to uncover the transferred electron number and the hydrogen peroxide yields of Fe_7S_8/NSC. As depicted in Fig. 5*b*, the electron transfer number is about 3.96–3.99 over the potential ranging from 0.2 to 0.8 V, accompanied with extremely low H_2O_2 yields (<5%), indicating a four-electron ORR pathway catalysed by sample Fe_7S_8/NSC [13].

Apart from the superior ORR activity, the OER performance of Fe_7S_8/NSC was also investigated. As presented in Fig. 5*c*, sample

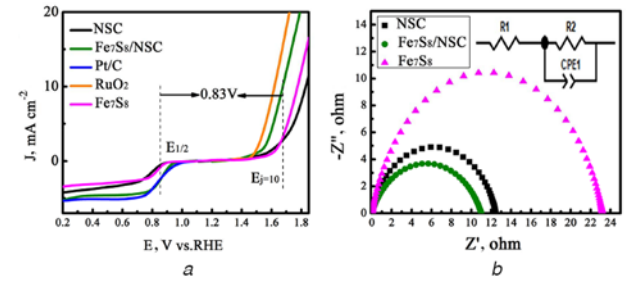

Fig. 6 *Overall LSV curves*
a In the whole ORR and OER region in 0.1 M KOH
b Electrochemical impedance spectroscopies of all samples

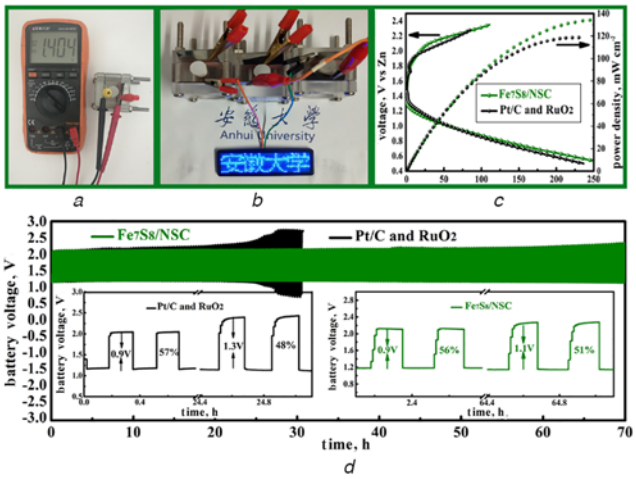

Fig. 7 *Performances of ZABs based on the as-fabricated samples*
a Open circuit voltage of ZAB
b Optical picture of a LED powered by three Fe_7S_8/NSC based ZABs in series
c Charge–discharge polarisation curve of ZAB
d Galvanostatic discharge–charge cycle profiles of the assembled liquid ZAB based on Fe_7S_8/NSC and Pt/C–RuO_2 mixed catalysts at 10 mA cm^{-2}

Fe_7S_8 exhibits an overpotential of 560 mV at a current density of 10 mA cm^{-2} ($E_j=10$), which is close to NSC (600 mV), and worse than other reported Fe_7S_8 catalysts such as Fe_7S_8 nanosheets in [14], signifying its unsatisfactory performance in OER. While Fe_7S_8/NSC has a smaller overpotential of 450 mV, compared to that of RuO_2 (390 mV), demonstrating the excellent OER activity of Fe_7S_8/NSC. Thus, it is suggested that the embedding of Fe_7S_8 nanoparticles into NSC in this work is an effective method to improve the ORR and OER activities of catalysts. The corresponding Tafel slope of Fe_7S_8/NSC in Fig. 5*d* is calculated as 112 mV dec^{-1}, which is much lower than that of NSC (211 mV dec^{-1}), Fe_7S_8 (123 mV dec^{-1}), and is comparable to that of RuO_2 (88 mV dec^{-1}), also signifying a prominent OER kinetic process.

The potential difference ($\Delta E=E_{j=10}-E_{1/2}$) was further employed to estimate the bifunctional activities of catalysts. As seen in Fig. 6*a*, Fe_7S_8/NSC displays a ΔE value of 0.83 V, smaller than or comparable to that of the other reported catalysts [15, 16]. Moreover, electrochemical impedance spectroscopy technology was applied to assess the electron transfer resistance of NSC, Fe_7S_8, and Fe_7S_8/NSC. As depicted in Fig. 6*b*, Fe_7S_8/NSC exhibits a lower R_{ct} value of 11.1 Ω compared to that of NSC (12.4 Ω), and Fe_7S_8 (23.1 Ω), indicating its higher charge transfer capacity. Therefore, Fe_7S_8/NSC exhibits outstanding electrocatalytic activity in ORR/OER, which is mainly ascribed to the peculiar 3D

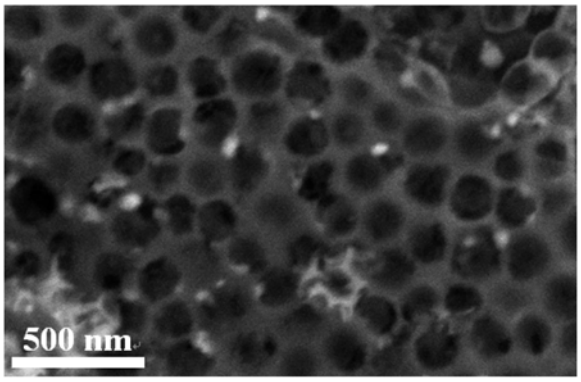

Fig. 8 *Typical SEM image of Fe_7S_8/NSC after 195 cycles*

interconnected porous structure, the codoping of nitrogen and sulphur atoms, as well as the synergistic effects between Fe_7S_8 nanoparticles and NSC framework.

To examine the utility of the Fe_7S_8/NSC catalyst, a liquid ZAB was manufactured. As depicted in Fig. 7*a*, the primary ZAB fabricated with Fe_7S_8/NSC exhibits a high open-circuit voltage of 1.404 V. Remarkably, three ZABs connected in series were adequate to light a light-emitting display (LED) screen (Fig. 7*b*). Fig. 7*c* further exhibits the charge–discharge polarisation and corresponding power density performances of the as-prepared ZABs. Clearly, the Fe_7S_8/NSC-based device shows a smaller potential gap than that of the ZAB based on commercial $Pt/C + RuO_2$, signifying higher efficiency of the charge–discharge process. Moreover, the peak power density of the Fe_7S_8/NSC air cathode is calculated to be 135 mW cm^{-2}, also outperforms that of $Pt/C + RuO_2$ (120 mW cm^{-2}). Additionally, the stability of the ZAB was evaluated by discharging–charging cycles at 10 mA cm^{-2}, as illustrated in Fig. 7*d*. After the test for 65 h (195 cycles), there is no obvious potential change in Fe_7S_8/NSC based ZAB, and the voltaic efficiency changes slightly from 56% (first cycle) to 51% (195th cycle). In contrast, a gradual increase of voltage gap is observed in the $Pt/C + RuO_2$ battery, with the voltaic efficiency changing from 57% (first cycle) to 48% only after 75 cycles. Furthermore, the SEM images of Fe_7S_8/NSC after cycling were also measured to confirm the structural stability. As shown in Fig. 8, after 195 cycles, the Fe_7S_8/NSC catalyst presents a similar structure with that illustrated in Fig. 1*c*, suggesting the pretty good structural stability of Fe_7S_8/NSC. The above performances suggest that Fe_7S_8/NSC has a promising application as an efficient bifunctional catalyst in ZAB.

4. Conclusions: In summary, we have developed an effective strategy for synthesising Fe_7S_8 nanoparticles embedded in N, S co-doped porous carbon (NSC) matrix as a bifunctional catalyst. The as-obtained Fe_7S_8/NSC exhibits a remarkable ORR activity, superior to that of Pt/C. Moreover, the OER activity of Fe_7S_8/NSC is comparable to that of RuO_2. The outstanding ORR/OER performance is mainly ascribed to the interconnected porous network architecture with a high specific surface area, the doping effects of nitrogen and sulphur atoms, and the synergistic reaction between highly active Fe_7S_8 and NSC. Notably, working as the air cathode, the Fe_7S_8/NSC catalyst has potential in ZAB as an efficient bifunctional catalyst with the high power density and appreciable stability.

5. Acknowledgment: This work was financed by the National Natural Science Foundation of China (51672001).

6 References

[1] Li Y.G., Dai H.J.: 'Recent advances in zinc-air batteries', *Chem. Soc. Rev.*, 2014, **43**, (15), pp. 5257–5275
[2] Xu H.M., Ci S.Q., Ding Y.C., *ET AL.*: 'Recent advances in precious metal-free bifunctional catalysts for electrochemical conversion systems', *J. Mater. Chem. A*, 2019, **7**, (14), pp. 8006–8029
[3] Cai X.Y., Lai L.F., Lin J.Y., *ET AL.*: 'Recent advances in air electrodes for Zn-air batteries: electrocatalysis and structure design', *Mater. Horiz.*, 2017, **4**, (6), pp. 945–976
[4] Fu G.T., Lee J.M.: 'Ternary metal sulfides for electrocatalytic energy conversion', *J. Mater. Chem. A*, 2019, **7**, (16), pp. 9386–9405
[5] Cao Z.Q., Wu M.Z., Hu H.B., *ET AL.*: 'Monodisperse Co_9S_8 nanoparticles in situ embedded within N, S-codoped honeycomb-structured porous carbon for bifunctional oxygen electrocatalyst in a rechargeable Zn–air battery', *NPG Asia Mater.*, 2018, **10**, pp. 670–684
[6] Cui H.J., Zhou Z., Jia D.Z.: 'Heteroatom-doped graphene as electrocatalysts for air cathode', *Mater. Horiz.*, 2017, **4**, (1), pp. 7–19
[7] Cantu J., Gonzalez L.E., Goodship J., *ET AL.*: 'Removal of arsenic from water using synthetic Fe_7S_8 nanoparticles', *Chem. Eng. J.*, 2016, **290**, pp. 428–437
[8] He Q.M., Rui K., Yang J.H., *ET AL.*: 'Fe_{7S_8} nanoparticles anchored on nitrogen-doped graphene nanosheets as anode materials for high-performance sodium-ion batteries', *ACS Appl. Mater. Interfaces*, 2018, **10**, (35), pp. 29476–29485
[9] Qiao X.C., Jin J.T., Fan H.B., *ET AL.*: 'In situ growth of cobalt sulfide hollow nanospheres embedded in nitrogen and sulfur co-doped graphene nanoholes as a highly active electrocatalyst for oxygen reduction and evolution', *J. Mater. Chem. A*, 2017, **5**, (24), pp. 12354–12360
[10] Liu W.W., Zhang J., Bai Z.Y., *ET AL.*: 'Controllable urchin-like $NiCo_2S_4$ microsphere synergized with sulfur-doped graphene as bifunctional catalyst for superior rechargeable Zn-air battery', *Adv. Funct. Mater.*, 2018, **28**, (11), p. 1706675
[11] Tompsett G.A., Krogh L., Griffin D.W., *ET AL.*: 'Hysteresis and scanning behavior of mesoporous molecular sieves', *Langmuir*, 2005, **21**, (18), pp. 8214–8225
[12] Wang B.B., Pan J.Q., Jiang Z.Y., *ET AL.*: 'The bimetallic iron-nickel sulfide modified g-C_3N_4 nano-heterojunction and its photocatalytic hydrogen production enhancement', *J. Alloys Compd.*, 2018, **766**, pp. 412–428
[13] Chen S.M., Cheng J.Y., Ma L.T., *ET AL.*: 'Light-weight 3D Co-N-doped hollow carbon spheres as efficient electrocatalysts for rechargeable zinc-air batteries', *Nanoscale*, 2018, **10**, (22), pp. 10412–10419
[14] Chen S.C., Kang Z.X., Zhang X.D., *ET AL.*: 'Highly active Fe sites in ultrathin pyrrhotite Fe_7S_8 nanosheets realizing efficient electrocatalytic oxygen evolution', *ACS Cent. Sci.*, 2017, **3**, (11), pp. 1221–1227
[15] Liu X., Wang L., Yu P., *ET AL.*: 'A stable bifunctional catalyst for rechargeable zinc-air batteries: iron-cobalt nanoparticles embedded in a nitrogen-doped 3D carbon matrix', *Angew. Chem., Int. Ed.*, 2018, **57**, (49), pp. 16166–16170
[16] Yin J., Li Y.X., Lv F., *ET AL.*: 'NiO/CoN porous nanowires as efficient bifunctional catalysts for Zn-air batteries', *ACS Nano*, 2017, **11**, (2), pp. 2275–2283

doi: 10.1049/mnl.2019.0763